

Hyper-efficient superconducting filterbanks with impedance-defined spectral resolution for millimeter-wave spectroscopy

O. Jeong^{1,2}¹CNRS-UCB International Research Laboratory, Centre Pierre Binétry, IRL 2007, CPB-IN2P3, Berkeley, CA 94720, USA²Lawrence Berkeley National Laboratory, 1 Cyclotron Road, Berkeley, CA 94720, USA

(*Electronic mail: objeong@lbl.gov)

(Dated: 20 March 2026)

We present a high-efficiency, high resolution on-chip filterbank spectrometer designed for line intensity mapping and broadband wave-like dark matter searches. This spectrometer maximizes sensitivity to the faint, aggregate cosmic signal for line intensity mapping while providing redshift precision necessary to resolve the clustering of large-scale structure. For broadband dark matter searches, it partitions broadband signals into narrow frequency bins that directly correspond to dark matter masses, allowing signal frequency to be mapped with high precision to the particle's mass. Existing superconducting filterbank architectures used by the mm-wave community are limited by a 50% inherent efficiency limit and are highly sensitive to thin-film dielectric loss. The design presented in this paper addresses these bottlenecks by eliminating the termination resistor and employing a niobium-on-silicon coplanar waveguide resonant structures for the filterbanks. Sonnet electromagnetic simulations of a 10-channel device around 90 GHz demonstrates >74% per channel efficiency and a resolving power of $R = 1211 \pm 105$. Sensitivity analyses confirm that the design is robust against typical fabrication uncertainties with the exception of dielectric thickness, providing a scalable technology solution for the next generation of millimeter-wave spectroscopic experiments.

I. INTRODUCTION

High resolution spectroscopy in the millimeter-wave regime offers a unique window into rich cosmological, astronomical, and fundamental physics information. Line intensity mapping (LIM) is an emerging method which measures the integrated emission of atomic and molecular lines from galaxies to map the universe in three dimensions. By observing large-scale structure (LSS) in unprecedented volumes of the observable universe, LIM enables the study of fundamental topics in cosmology such as multi-field inflation and dynamic dark energy. Another powerful application is with broadband wave-like dark matter (DM) search experiments such as BREAD.¹ A high-resolution spectrometer can partition broadband signal into narrow frequency bins, which correspond directly to discrete DM mass intervals. Because the signal frequency is determined by DM mass, fine spectral resolution provides high-fidelity mapping of DM mass.

Several spectrometer technologies have been developed, including Fourier transform spectrometers,² diffraction gratings,³ on-chip diffraction gratings,⁴ and on-chip filterbank spectrometers.⁵⁻⁹ Among these, on-chip filterbanks are particularly promising for LIM due to their inherent scalability required for deep surveys.¹⁰ Their compact physical footprint allows for large pixel count focal planes and their ability to couple hundreds of narrow-band spectroscopic channels to a single feedline enables probing a large range of frequencies, and thus redshifts, simultaneously with a single pixel. While technologies such as SuperSpec⁵ and DESHIMA⁶ have demonstrated the viability of this design approach, existing implementations are limited in optical efficiency (η) and resolving power ($R = v/\delta v$) due to both fundamental circuit design constraints and strong dependence on material loss properties within the circuit.

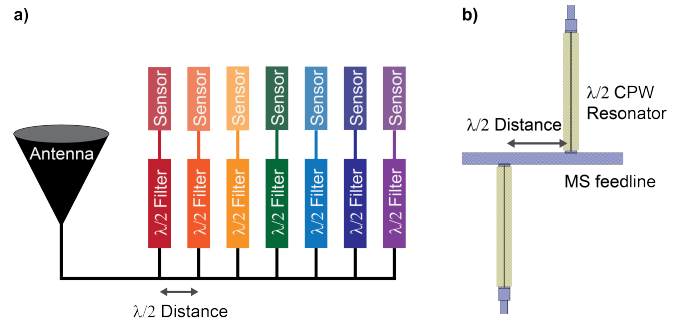


FIG. 1. (a) A design schematic of the filterbank spectrometer and (b) a CAD drawing of two adjacent filterbanks, with light purple representing niobium strips and olive representing exposed silicon substrate between the Nb signal line and ground plane of the coplanar waveguide. This design is inspired by the cochlear signal partitioning in the human ear.

In this paper, we present a new filterbank architecture that achieves a significant improvement in η and R . This design achieves $\eta > 0.74$ per channel and $R = 1211 \pm 105$ while being significantly more robust against dielectric loss than conventional on-chip circuit designs. We describe the governing circuit principles, verify performance via electromagnetic simulations, and provide a detailed sensitivity analysis regarding fabrication uncertainties.

II. CIRCUIT DESIGN PRINCIPLES

The circuit architecture of this spectrometer is inspired by the frequency-selective mechanics of the human ear, where power propagates along a common transmission-line that is coupled to a sequence of log-periodically spaced resonant

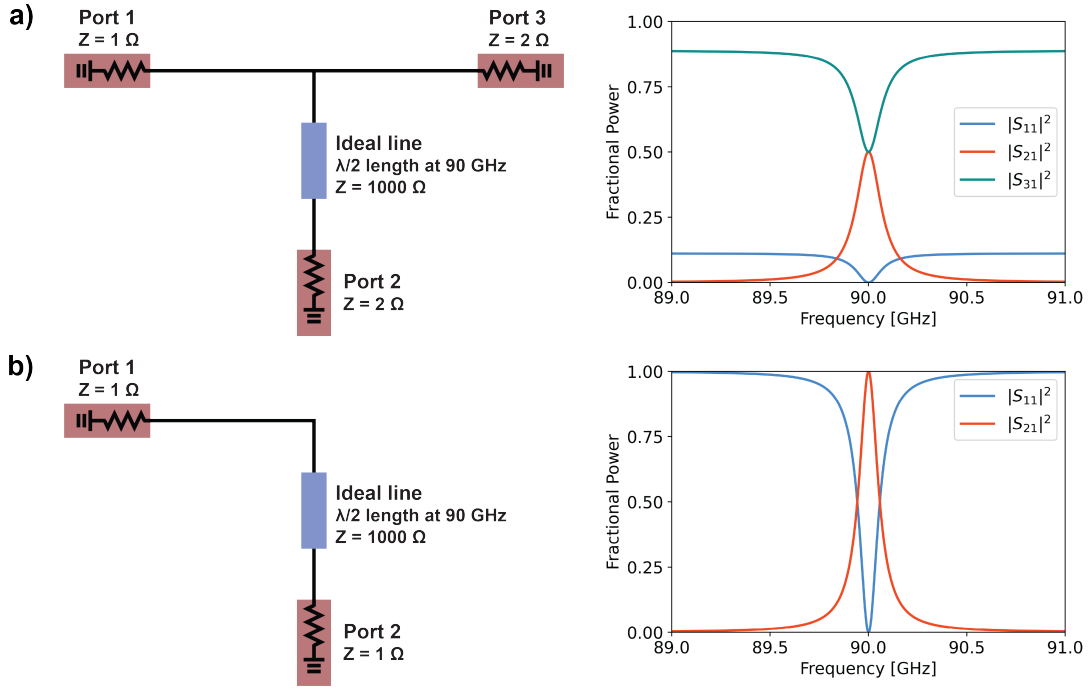


FIG. 2. Circuit model and resulting filter efficiency using Quite Universal Circuit Simulator (QUCS) for (a) a representative circuit of existing technologies with a termination resistor and (b) the circuit principle employed for this technology without a termination resistor. While (a) shows that power is split evenly between the filter and termination resistor at the resonant frequency with $|S_{21}|^2$ capped at 0.5, (b) shows that all of the power is transmitted through the filter with $|S_{21}|^2 = 1$. Port impedances are set for maximal power transmitted to Port 2.

bandpass filters (see Fig. 1).^{11–14} In this implementation, signal from the sky is captured by an antenna and coupled into the main transmission feedline. As the signal propagates along the feedline, it encounters a sequence of shunts arranged in descending order of frequency. Each shunt comprises a distributed half-wave resonant structure with a common resolving power, R . These resonators are designed to selectively couple power within a narrow fractional bandwidth at unique, staggered frequencies, effectively channelizing the incoming broadband signal for high-resolution spectroscopy. The resolving power of such filterbank is determined by its quality factor Q , defined as:

$$\frac{1}{R} = \frac{1}{Q} = \frac{1}{Q_{\text{feed}}} + \frac{1}{Q_{\text{det}}} + \frac{1}{Q_{\text{loss}}}, \quad (1)$$

where Q_{feed} is the coupling quality factor between the feedline and filter, Q_{det} is the coupling quality factor between the filter and detector, and Q_{loss} is the quality factor broadly describing loss in the resonator. The resonator channels are placed at frequency ν_i where the length of the i -th resonator filter for a log-periodic design with constant R is given by

$$l_i = l_0 \cdot r^i \quad (2)$$

$$r = 1 + \frac{1}{R\Sigma}, \quad (3)$$

where Σ is the oversampling factor.

Existing mm-wave spectrometers suffer from an efficiency-resolution bottleneck driven by two primary circuit design el-

ements. First, conventional on-chip filterbanks employ a resistive terminator after the final channel to prevent standing waves and residual reflections;¹⁵ however, this design choice immediately imposes an inherent efficiency cap of $\eta = 50\%$ per channel, given by Eq. 4 when $R \gg Q_{\text{loss}}$, before accounting for any material dissipation:¹⁶

$$\eta = \frac{1}{2} \left(1 - \frac{R}{Q_{\text{loss}}} \right)^2. \quad (4)$$

The highest achieved optical efficiency reported is 16%.⁷ Note that spectrometers can oversample across the band to boost the cumulative efficiency of the spectrometer following,

$$\langle \eta_{\text{tot}} \rangle \approx \Sigma \cdot \langle \eta_i \rangle, \quad (5)$$

where $\langle \cdot \rangle$ denotes the mean. However, this comes at the cost of larger channel count, N_{ch} , following

$$N_{\text{ch}} = \Sigma \cdot R \cdot \log \left(\frac{\nu_{\text{max}}}{\nu_{\text{min}}} \right), \quad (6)$$

for log-spaced filters between frequencies ν_{min} and ν_{max} (see Appendix A for more detail). Furthermore, there are diminishing gains from pushing the oversampling factor beyond Nyquist sampling ($\Sigma = 2$) as one pays the penalty in detector noise for splitting signal at a single frequency between more and more detectors.¹⁷ This motivates the development of a filterbank technology with $\eta > 50\%$ as it ensures manageable detector counts and optimal noise performance.

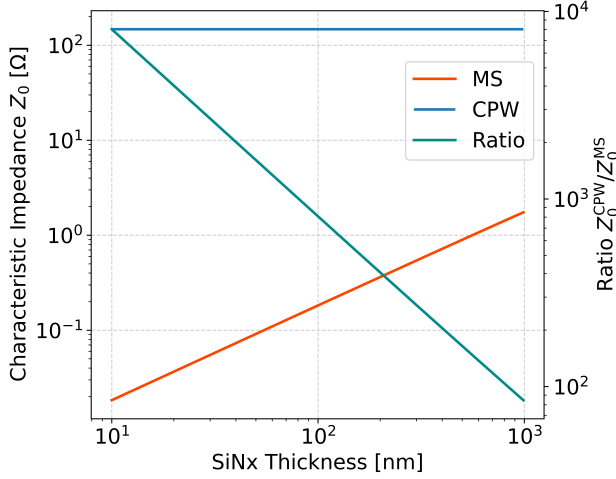


FIG. 3. Impedance ratio as a function of dielectric thickness, assuming a SiNx dielectric interlayer ($\epsilon_r = 8.6$). Tab. I shows the parameters used in these Z_0 calculations. Z_0^{MS} decreases with SiNx thickness and therefore the ratio $Z_0^{\text{CPW}}/Z_0^{\text{MS}}$. Because the resolving power of these filterbanks scales with this ratio, decreasing the SiNx thickness leads to higher R .

Second, current designs rely on half-wave microstrip (MS) resonators^{5,7,18} which require lossy amorphous dielectric inter-layers. This makes the resolving power R and efficiency η strongly sensitive to the material's loss tangent ($\tan \delta$), leading to significant risk of performance degradation during fabrication, evidenced by recent implementations where unexpected deviations of silicon nitride (SiNx) properties caused resolution to drop from a target of 100 to $R = 33$.¹⁹ The spectrometer presented in this paper addresses these problems with two targeted modifications.

The problem of inherent limit of optical efficiency is addressed by final eliminating the termination resistor on the feedline (illustrated in Fig. 1a). The standing wave environment is treated as a deterministic design feature by spacing resonator shunts at $\lambda/2$ intervals, ensuring uncaptured signal reflects back to interfere coherently with incoming signal. This creates a zero-loss manifold where power is recycled and efficiency of each channel is boosted. Cosmic microwave background detectors have successfully implemented the design without a termination resistor.^{11,12,20} Fig. 2b demonstrates that eliminating the final termination resistor increases the maximum efficiency of a resonant filter from 50% to 100%.

The dependence of η and R on material loss is suppressed by utilizing a coplanar waveguide (CPW) architecture with niobium (Nb) metallization patterned directly onto low-loss single-crystal silicon (Si). Unlike MS designs^{5,7,19} which require lossy amorphous dielectrics, the CPW geometry allows fields to propagate primarily through the underlying low-loss substrate. While CPW structures can be susceptible to radiative loss, it can be suppressed using bridges when necessary to maintain equipotential state between the CPW ground planes.

Quality factors Q_{feed} and Q_{det} are governed by the impedance ratio between the high-impedance CPW shunt and the low-impedance MS feedline. The characteristic impedance of the MS line is given by:²¹

$$Z_0^{\text{MS}} = \frac{120\pi}{\sqrt{\epsilon_{\text{eff}}^{\text{MS}} (w/t + 1.393 + 0.667 \log(w/t + 1.444))}}, \quad (7)$$

where w and t are the trace width and dielectric thickness, and the effective relative permittivity is

$$\epsilon_{\text{eff}}^{\text{MS}} = \frac{\epsilon_r + 1}{2} + \frac{\epsilon_r - 1}{2\sqrt{1 + 12t/w}}. \quad (8)$$

Similarly, the characteristic impedance for CPW is given by:²²

$$Z_0^{\text{CPW}} = \frac{30\pi}{\sqrt{\epsilon_{\text{eff}}^{\text{CPW}}}} \frac{K(k'_0)}{K(k_0)}, \quad (9)$$

where $K(k)$ is the complete elliptical integral of first kind and $\epsilon_{\text{eff}}^{\text{CPW}}$ is the effective relative permittivity described by

$$\epsilon_{\text{eff}}^{\text{CPW}} = \frac{1 + \epsilon_r}{2}, \quad (10)$$

with $k_0 = \frac{s}{s+2d}$ and $k'_0 = \sqrt{1 - k_0^2}$. Here, s is the width of the signal line trace and d is the width of the gap between this trace and the nearest ground plane edge. R is tuned through the circuit element geometries, as adjusting the geometric parameters varies the ratio of CPW and MS impedances.

Fig. 3 illustrates this tuning mechanism, where Z_0^{MS} decreases and the impedance ratio $Z_0^{\text{CPW}}/Z_0^{\text{MS}}$ subsequently increases as the SiNx thickness t is reduced. The steep sensitivity of this ratio to t is a direct result of the effect of electromagnetic field confinement. As the dielectric layer thins, the fields are increasingly concentrated within the SiNx volume rather than the surrounding vacuum. This leads to a non-linear surge in capacitance per unit length, which drives the MS impedance Z_0^{MS} downward. Because Z_0^{CPW} is independent of t , this leads to a divergence in the impedance ratio, and consequently R , observed at low values of t .

III. SIMULATION RESULTS

Using typically achievable feature sizes for both CPW and MS geometries (see Tab. I for nominal values), the planar structures for a 10-channel filterbank spectrometer with $\Sigma = 1$, sampling between 89.6 and 90.4 GHz were implemented in the Sonnet electromagnetic simulation environment. Note that the SiNx thickness of 50 nm is thinner than the typical MS interlayer dielectric used in millimeter-wave RF circuits. The 10 channels are differentiated solely by the physical length of

TABLE I. Design parameters and nominal values for the filterbank spectrometer as implemented in Sonnet EM simulations. Refer to Fig. 4 for a cross-sectional illustration showing these parameters.

Component	Parameter	Value
CPW Resonator	Signal strip width (s)	$2 \mu\text{m}$
	Ground plane gap width (d_{GP})	$80 \mu\text{m}$
	Si relative permittivity	11.7
	Si loss tangent ²³	1×10^{-5}
MS Feedline	Strip width (w)	$70 \mu\text{m}$
	SiNx thickness (t)	50 nm
	SiNx relative permittivity ^a	8.6
	SiNx loss tangent	1×10^{-3}
Nb Superconductor	Surface inductance (L_s) ^b	$0.15 \text{ pH}/\square^{\text{c}}$

^a High relative permittivity SiNx is developed by Suzuki *et al.*²⁴ for cosmic microwave background measurement applications.

^b Surface inductance is utilized within the Sonnet environment to account for the kinetic inductance of the superconducting thin film.²⁵

^c Measured using resonator at 6 GHz by the Lawrence Berkeley National Laboratory Superconducting Detector Group.

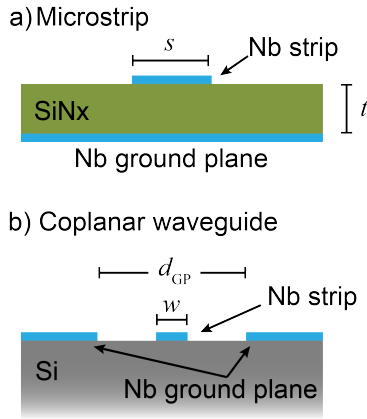


FIG. 4. Cross-sectional illustration of the (a) MS and (b) CPW architectures utilized in this filterbank design. Labels correspond to the design parameters and material layers detailed in Tab. I.

their respective CPW half-wave shunts and placed at $\lambda/2$ distance from each other along the feedline, defined for the i -th channel within Sonnet following

$$l_i^{\text{CPW}} = l_0^{\text{CPW}} + i \cdot dl^{\text{CPW}} \quad (11)$$

$$l_i^{\text{MS}} = l_0^{\text{MS}} + i \cdot dl^{\text{MS}} \quad (12)$$

for $i \in \{0, 1, \dots, 9\}$. l_i^{CPW} and l_i^{MS} are the length of the i -th resonator and distance between the i -th and $(i+1)$ -th resonator, respectively, for $l_0^{\text{CPW}} = 702.5 \mu\text{m}$ and $l_0^{\text{MS}} = 267.5 \mu\text{m}$. In this study, frequency intervals deviate from the ideal scaling in Eq. 2 due to the high computational cost of the required simulation box resolution. Instead, a constant physical length increment dl^{CPW} was implemented following Eq. 11. Because this fixed length step does not scale with the narrowing channel bandwidth, $\delta v_i = v_i/R$, it results in a widening gap between adjacent channel bins and therefore larger amplitude of fluctuation of the total efficiency along descending frequency.

Fig. 5 shows the simulated performance of this filterbank design for a setup with and without dielectric absorption. The lossless case isolates the intrinsic channel behavior, highlighting the rising ripple amplitude in the cumulative transmitted efficiency due to the mismatch between the shrinking channel δv_i and the constant dl^{CPW} steps of the resonators. Additionally, the impact of absorption loss becomes increasingly pronounced at lower frequencies. This is a direct consequence of the high-frequency channels being placed upstream on the feedline, which forces lower-frequency signals to propagate further along the lossy feedline before being channelized. With absorption loss taken into account, this spectrometer achieves greater than 74% efficiency per channel and a resolving power of $R = 1211 \pm 105$. These values are extracted by fitting a skewed Lorentzian to the simulated S-parameter output of Sonnet.

The robustness of the filterbanks against fabrication uncertainties is evaluated by performing a parameter sweep using a representative 5-channel sub-unit. To understand the possible degradation of the filterbank performance due to fabrication errors, the dependence of η and R for the middle channel on the design parameters with the largest fractional uncertainties is examined - the width of the CPW signal strip s , the MS SiNx thickness t , SiNx ϵ_r , and SiNx $\tan \delta$. While all parameters are varied by $\pm 10\%$, SiNx $\tan \delta$ is varied between 10^{-3} to 10^{-2} to account for possible degradation seen by Benson *et al.*¹⁹ Fig. 6 shows the peak η and R for the channel with respect to variations from the fiducial values of these design parameters.

The analysis demonstrates that the spectrometer performance is largely insensitive to variations in CPW signal strip s , SiNx ϵ_r , and SiNx $\tan \delta$. However, deviations exceeding 5% in SiNx thickness causes a sharp decline in both η and R . As illustrated in Fig. 3, this sensitivity arises from the strong dependence of the MS electromagnetic properties, and consequently the shunt $\lambda/2$ spacing scheme, on the dielectric thickness. This suggests that the nominal SiNx thickness should be increased to reduce its relative sensitivity to fabrication tolerances at the cost of an already high R . A similar mechanism underpins the system's sensitivity to the SiNx ϵ_r , which represents the next most significant design dependency. Because shifts in ϵ_r also disrupts the phase-matching of the shunt intervals, a 10% increase in relative permittivity results in a 17% reduction in peak η and a 36% decrease in R . However, even under such extreme degradation, both η and R remain high, indicating that the architecture possesses sufficient inherent performance margin to absorb substantial deviation in SiNx ϵ_r from the nominal value.

Notably, the channel performance remains insensitive to degradation in the SiNx $\tan \delta$; even a tenfold increase in $\tan \delta$ results in only a 5% reduction in R and a 13% decrease in peak η . As expected, this provides a significant safety margin against possible runaway increase in SiNx $\tan \delta$ that has historically hindered existing technologies. Ultimately, this architecture proves highly robust against most critical fabrication uncertainties because the primary resonant structure - the CPW with Nb metalization directly on low-loss Si substrate - is decoupled from the lossier dielectric layer.

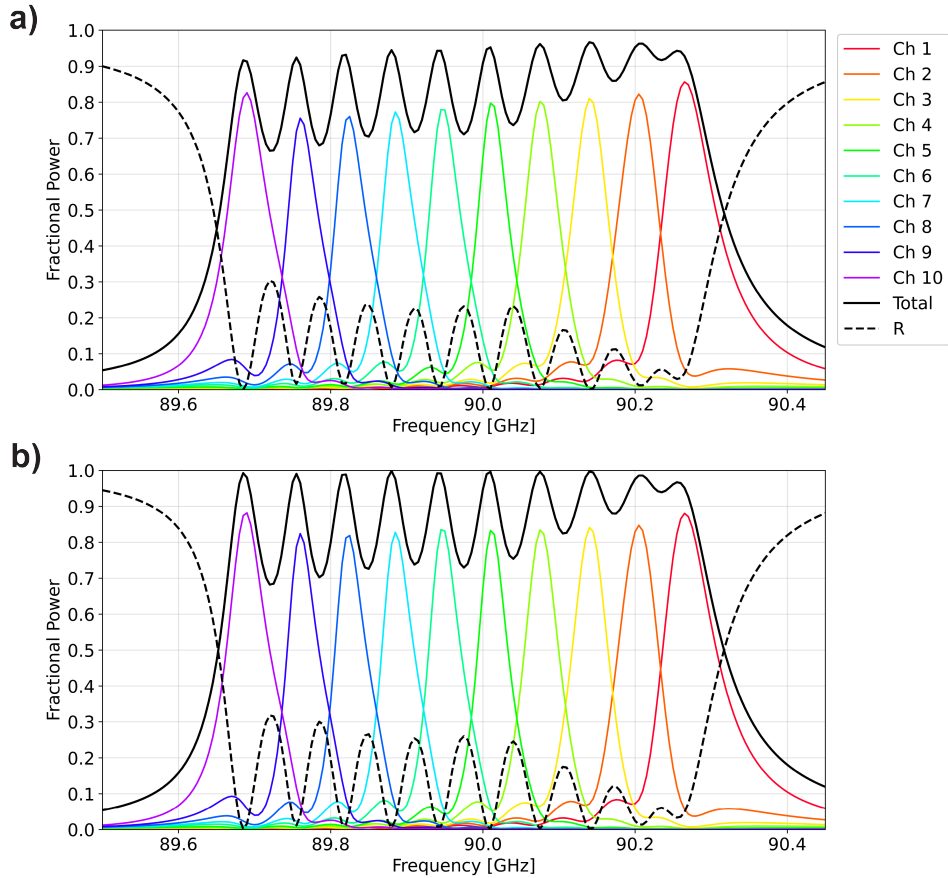


FIG. 5. Fractional transmitted power (solid) and reflected (dashed) of a 10 channel filterbank design for (a) realistic and (b) lossless dielectric layers, simulated using Sonnet simulation environment. The individual channels of the realistic design show $\eta > 0.74$ and $R = 1211 \pm 105$.

IV. CONCLUSION

We have presented a superconducting filterbank architecture that achieves high per-channel efficiency ($\eta > 0.74$) and high resolving power ($R = 1211 \pm 105$) through two fundamental design choices: the elimination of the termination resistor on the feedline after the last filterbank and the implementation of CPW resonators on a low-loss single-crystal Si substrate. Removing the termination resistor eliminates a major source of signal loss, while the CPW architecture de-risks the design against the material uncertainties of thin-film dielectrics. Sensitivity simulations confirm that this technology is robust against common fabrication tolerances, with the notable exception of the SiNx thickness. This motivates the next iteration of this design to increase thickness at the cost of an already high R . As a next step, we will fabricate and characterize this design, the results of which will be detailed in forthcoming publications.

ACKNOWLEDGMENTS

The author wishes to thank their colleagues - Adrian T. Lee, Martin White, and Kaja Rotermund - for their useful discus-

sions.

Appendix A: Oversampling and Total Spectrometer Efficiency

While the individual channel efficiency η is a fundamental metric of the filterbank architecture, the total power captured across the observing band is enhanced by the spectral overlap of adjacent channels. The relationship between channel density and the cumulative transmitted power, introduced in Section II, can be numerically validated by comparing filterbank configurations with varying oversampling factor Σ . As defined by Eq. 5, the cumulative efficiency η_{tot} is a summation of individual channel responses. In a perfectly continuous limit, this summation fills the spectral gaps between adjacent resonators, recovering power that would otherwise be lost.

To illustrate this effect, we compare two toy filterbank models simulated in QUCS, both covering ~ 0.8 GHz bandwidth around 90 GHz targeted in the Sonnet spectrometer design. In the case of $\Sigma = 1$ sampling, as shown in Fig. 7a, the filters are spaced such that they only nominally overlap, mirroring the baseline configuration of the device. This manifests as periodic dips in the total transmitted power between channel peaks and a lower average cumulative efficiency across the

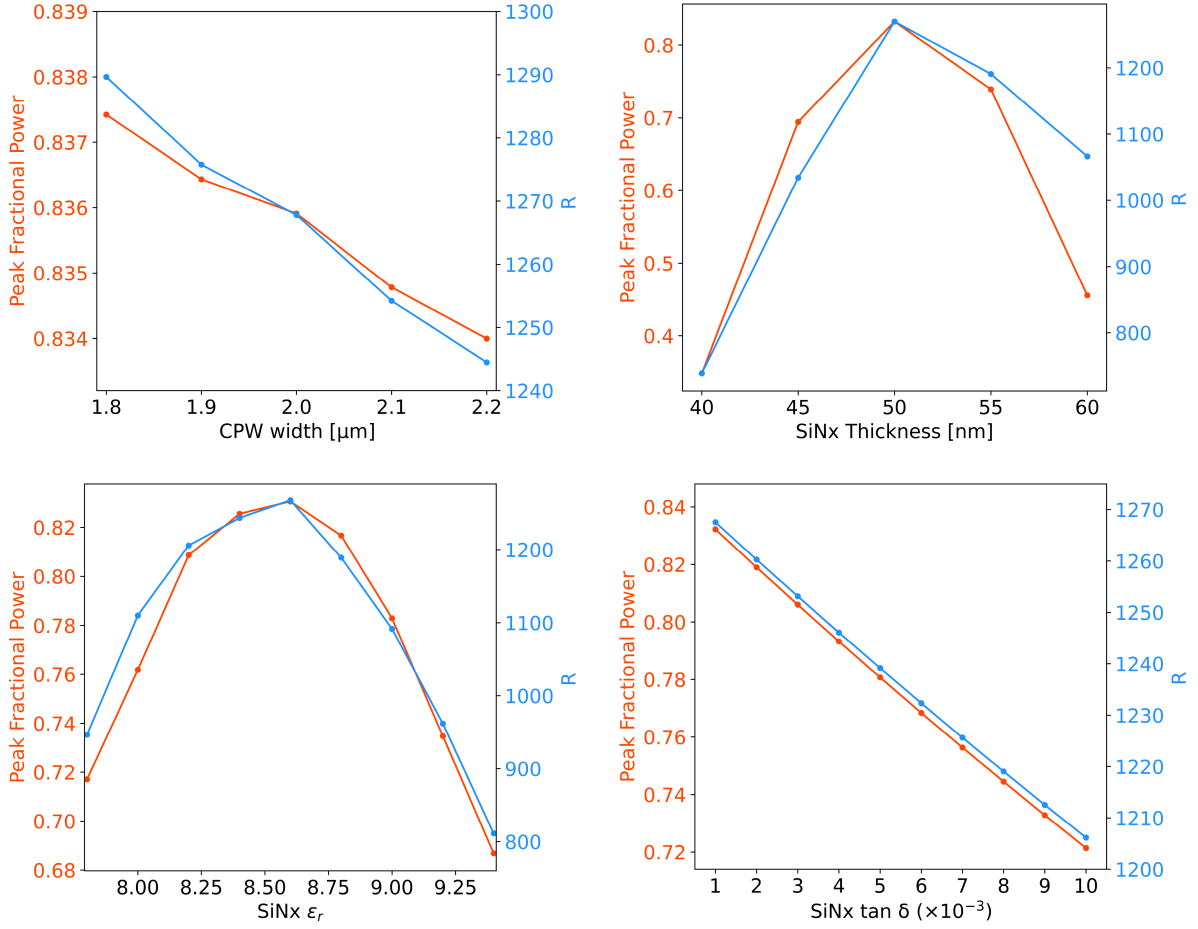


FIG. 6. Sensitivity study of the middle channel of a representative 5-channel sub-unit. The dependence of η and R on design parameters with the largest fractional uncertainties is studied by performing a parameter sweep in Sonnet. The design parameters studied are the width of the CPW signal line (top-left), SiNx thickness (top-right), SiNx relative permittivity (bottom-left), and SiNx loss tangent (bottom-right).

band. When the oversampling factor is increased to $\Sigma = 1.5$ as shown in Fig. 7b, the channel density increases by 50% while the total bandwidth remains the same. This increased spectral overlap leads to smoother and higher average cumulative efficiency across the target band.

- ¹G. Hoshino, S. Knirck, M. H. Awida, *et al.* (GigaBREAD Collaboration), “First axionlike particle results from a broadband search for wavelike dark matter in the 44 to 52 μeV range with a coaxial dish antenna,” *Phys. Rev. Lett.* **134**, 171002 (2025).
- ²M. De Petris, S. De Gregori, B. Decina, L. Lamagna, and J. R. Pardo, “Atmospheric monitoring in the millimetre and submillimetre bands for cosmological observations: Casper2,” *MNRAS* **429**, 849–858 (2012), <https://academic.oup.com/mnras/article-pdf/429/1/849/3420237/sts380.pdf>.
- ³C.-T. Li, C. M. Bradford, A. Crites, J. Hunacek, T. Wei, J.-C. Cheng, T.-C. Chang, and J. Bock, “TIME millimeter wave grating spectrometer,” in *Millimeter, Submillimeter, and Far-Infrared Detectors and Instrumentation for Astronomy IX*, Vol. 10708, edited by J. Zmuidzinas and J.-R. Gao, International Society for Optics and Photonics (SPIE, 2018) p. 107083F.
- ⁴G. Cataldo, W.-T. Hsieh, W.-C. Huang, S. H. Moseley, T. R. Stevenson, and E. J. Wollack, “Micro-spec: an ultracompact, high-sensitivity spectrometer for far-infrared and submillimeter astronomy,” *Appl. Opt.* **53**, 1094–1102 (2014).
- ⁵R. J., P. S. Barry, C. M. Bradford, *et al.*, “Superspec: On-chip spectrometer

- design, characterization, and performance,” *J Low Temp Phys* **209**, 548–555 (2022).
- ⁶A. Endo, K. Karatsu, Y. Tamura, *et al.*, “First light demonstration of the integrated superconducting spectrometer,” *Nat Astron* **3**, 989–996 (2019).
- ⁷K. Karatsu *et al.*, “Deshima 2.0: A 200–400 ghz ultra-wideband integrated superconducting spectrometer,” (2026), arXiv:2601.21603 [astro-ph.IM].
- ⁸R. Nie, J. Filippini, E. Brooks, *et al.*, “A vacuum waveguide filter bank spectrometer for far-infrared astrophysics,” *Journal of Low Temperature Physics* **216**, 408–416 (2024).
- ⁹M. A. Koc, J. Ausermann, J. Beall, *et al.*, “Development of silicon micromachined waveguide filter-banks for on-chip spectrometers,” (2025), arXiv:2511.02756 [astro-ph.IM].
- ¹⁰K. S. Karkare, A. M. Dizgah, G. K. Keating, P. Breyse, and D. T. Chung, “Snowmass 2021 cosmic frontier white paper: Cosmology with millimeter-wave line intensity mapping,” (2022), arXiv:2203.07258 [astro-ph.CO].
- ¹¹R. O’Brien *et al.*, “A dual-polarized broadband planar antenna and channelizing filter bank for millimeter wavelengths,” *Journal of Low Temperature Physics* **102**, 063506 (2013).
- ¹²R. O’Brien, P. Ade, K. Arnold, J. Edwards, G. Engargiola, W. Holzappel, A. T. Lee, M. Myers, G. Rebeiz, P. Richards, and A. Suzuki, “A log-periodic channelizer for multichroic antenna-coupled tes-bolometers,” *IEEE Transactions on Applied Superconductivity* **21**, 180–183 (2011).
- ¹³C. J. Galbraith, R. D. White, L. Cheng, K. Grosh, and G. M. Rebeiz, “Cochlea-based rf channelizing filters,” *IEEE Transactions on Circuits and Systems I: Regular Papers* **55**, 969–979 (2008).

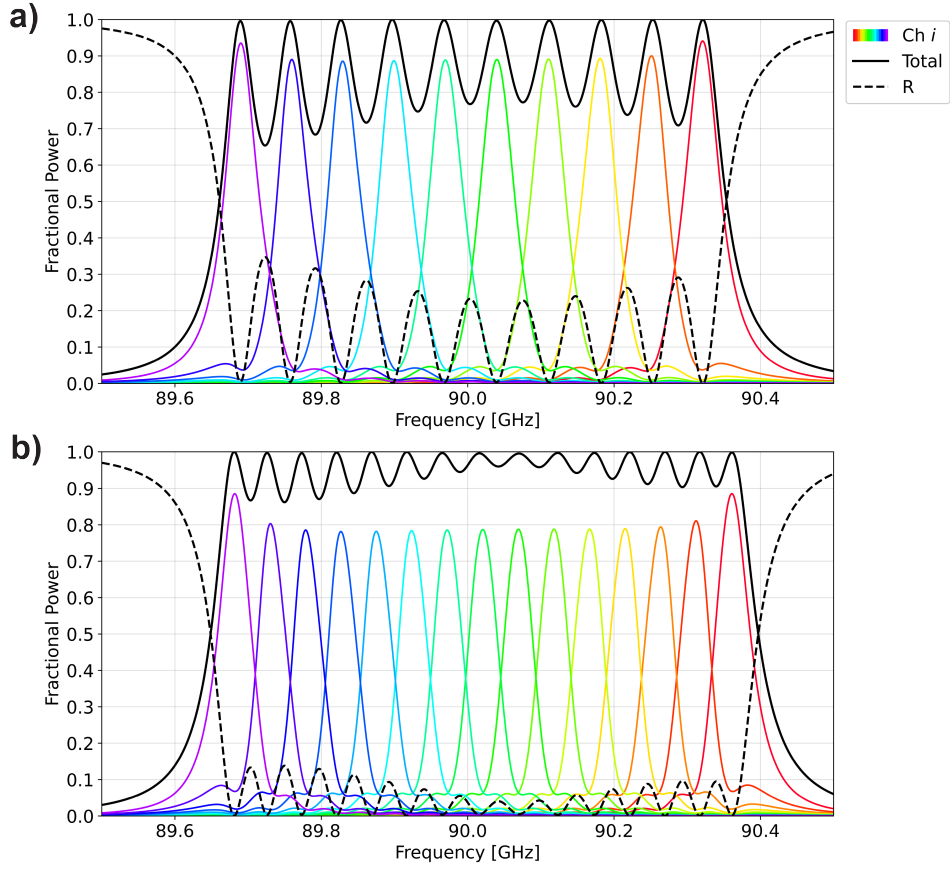


FIG. 7. Fractional transmitted power (solid) and reflected (dashed) of a (a) 10 channel, $\Sigma = 1$ filterbank design and (b) 15 channel, $\Sigma = 1.5$ design, simulated using QUCS. Cumulative efficiency (black, solid) is boosted by higher oversample factor.

- ¹⁴C. J. Galbraith and G. M. Rebeiz, “Higher order cochlea-like channelizing filters,” *IEEE Transactions on Microwave Theory and Techniques* **56**, 1675–1683 (2008).
- ¹⁵P. Barry, *On the development of SuperSpec; a Fully Integrated On-chip Spectrometer for Far-infrared Astronomy*, Ph.D. thesis, Cardiff University (2014).
- ¹⁶S. Hailey-Dunsheath, P. Barry, C. Bradford, *et al.*, “Optical measurements of superspec: A millimeter-wave on-chip spectrometer,” *Journal of Low Temperature Physics* **176**, 841–847 (2014).
- ¹⁷J. Wheeler, *Millimeter-Wave Galaxy Spectroscopy: SuperSpec On-Chip Spectrometer Technology Development and ALMA Observations of Molecular Gas In The Arp 220 Nucleus*, Ph.D. thesis, University of Colorado, Boulder (2019).
- ¹⁸K. Karkare, A. Anderson, P. Barry, *et al.*, “Spt-slim: A line intensity mapping pathfinder for the south pole telescope,” *Journal of Low Temperature Physics* **209**, 758–765 (2022).
- ¹⁹C. S. Benson, K. Fichman, M. Adamic, *et al.*, “Spectral characterization and performance of spt-slim on-chip filterbank spectrometers,” (2025), arXiv:2509.02245 [astro-ph.IM].
- ²⁰A. Suzuki, *Multichroic Bolometric Detector Architecture for Cosmic Microwave Background Polarimetry Experiments*, Ph.D. thesis, University of California, Berkeley (2013).
- ²¹D. M. Pozar, *Microwave Engineering*, 4th ed. (Wiley, 2011).
- ²²R. N. Simons, *Coplanar Waveguide Circuits, Components, and Systems* (Wiley, 2001).
- ²³J. Krupka, J. Breeze, A. Centeno, N. Alford, T. Claussen, and L. Jensen, “Measurements of permittivity, dielectric loss tangent, and resistivity of float-zone silicon at microwave frequencies,” *IEEE Transactions on Microwave Theory and Techniques* **54**, 3995–4001 (2006).
- ²⁴A. Suzuki, N. Cothard, A. Lee, *et al.*, “Commercially fabricated antenna-coupled transition edge sensor bolometer detectors for next-generation cosmic microwave background polarimetry experiment,” *Journal of Low Temperature Physics* **199**, 1158–1166 (2020).
- ²⁵A. R. Kerr, “Surface impedance of superconductors and normal conductors in EM simulators,” Electronics Division Internal Report No. 302 (NRAO, Charlottesville, VA, 1999) mMMA Memo No. 245.